Available online at www.sciencedirect.com

ScienceDirect

Geochimica et Cosmochimica Acta 170 (2015) 51–68

Geochimica et Cosmochimica Acta

www.elsevier.com/locate/gca

A novel determination of calcite dissolution kinetics in seawater

Adam V. Subhas [a,*], Nick E. Rollins [b], William M. Berelson [b], Sijia Dong [b], Jonathan Erez [c], Jess F. Adkins [a]

[a] California Institute of Technology, Pasadena, CA 91125, United States
[b] University of Southern California, Los Angeles, CA 90089, United States
[c] The Hebrew University, Jerusalem, Israel

Received 2 January 2015; accepted in revised form 11 August 2015; Available online 31 August 2015

Abstract

We present a novel determination of the dissolution kinetics of inorganic calcite in seawater. We dissolved ^{13}C-labeled calcite in unlabeled seawater, and traced the evolving $\delta^{13}C$ composition of the fluid over time to establish dissolution rates. This method provides sensitive determinations of dissolution rate, which we couple with tight constraints on both seawater saturation state and surface area of the dissolving minerals. We have determined dissolution rates for two different abiotic calcite materials and three different grain sizes. Near-equilibrium dissolution rates are highly nonlinear, and are well normalized by geometric surface area, giving an empirical dissolution rate dependence on saturation state (Ω) of:

$$\text{Rate } (\text{g/cm}^2/\text{day}) = 7.2 \pm 0.6 \cdot 10^{-4}(1-\Omega)^{3.9\pm0.1}.$$

This result substantiates the non-linear response of calcite dissolution to undersaturation. The bulk dissolution rate constant calculated here is in excellent agreement with those determined in far from equilibrium and dilute solution experiments. Plots of dissolution versus undersaturation indicates the presence of at least two dissolution mechanisms, implying a criticality in the calcite-seawater system. Finally, our new rate determination has implications for modeling of pelagic and seafloor dissolution. Nonlinear dissolution kinetics in a simple 1-D lysocline model indicate a possible transition from kinetic to diffusive control with increasing water depth, and also confirm the importance of respiration-driven dissolution in setting the shape of the calcite lysocline.

1. INTRODUCTION

Calcium carbonate minerals are a major component of the global carbon cycle. At steady state, alkalinity input to the oceans from terrestrial weathering and rivers is ultimately balanced by calcium carbonate burial in marine sediments. In the modern ocean, marine calcifiers produce at least four times more calcium carbonate than is needed to balance the terrestrial alkalinity source (Sigman and Boyle, 2000; Sarmiento and Gruber, 2006). This imbalance results in a large dissolution flux back into the ocean, from the water column and the sediments. Dissolution acts as a filter between calcium carbonate production and its eventual long-term preservation, and is the link between calcium carbonate cycling and the global alkalinity cycle. Marine calcifiers currently precipitate about 1 Gigaton (GT) of carbon per year in the surface ocean, a flux which over geological time has built up a sedimentary reservoir of $CaCO_3$ is about $48 \cdot 10^6$ GT of carbon (Sigman and Boyle, 2000). Today, atmospheric CO_2 concentrations are rising at

* Corresponding author. Tel.: +1 (626) 395 8647.
E-mail address: asubhas@gps.caltech.edu (A.V. Subhas).

http://dx.doi.org/10.1016/j.gca.2015.08.011
0016-7037/

geologically unprecedented rates (Stockner et al., 2013). The response and feedback of calcium carbonates to this perturbation is of major significance to our climate and environment. In the oceans, invasion of CO_2 leads to an increase of dissolved inorganic carbon (DIC), without a concomitant change in alkalinity. This shift in the DIC:Alkalinity ratio decreases surface ocean $[CO_3^{2-}]$ and saturation state; a decrease that will eventually propagate into the deep ocean. Because both precipitation and dissolution of calcite are sensitive to saturation state, the suppression of calcification in the surface ocean, and carbonate dissolution throughout the water column and in the sediments, are two ways in which calcium carbonate can buffer excess atmospheric pCO_2. With ~250 GT of anthropogenic carbon emitted since the preindustrial era (about one third of which has invaded the oceans, Sabine et al. (2004)), we are already significantly altering the surface ocean carbon cycle (Feely et al., 2012; Bednarsek et al., 2014).

Calcium carbonate dissolution will potentially neutralize all fossil fuel-derived CO_2 introduced into the ocean. The neutralization timescale is a subject of some debate (Archer et al., 1998; Boudreau et al., 2010a; Ilyina and Zeebe, 2012), and is coupled to the timescale of ocean circulation, sediment bioturbation, and the kinetics of dissolution itself. Since ocean acidification is occurring more rapidly than ever documented in geological history, we need to understand the kinetics of calcium carbonate dissolution, and its role in the buffering of anthropogenic CO_2 emissions, to best predict the fate of fossil fuel CO_2 that invades the ocean.

It is surprising that despite the quantity and caliber of research on calcium carbonate dissolution, there is still a major debate over the basic formulation of a dissolution rate law. The kinetics of calcium carbonate dissolution are typically described by the equation:

$$\text{Rate} = k(1-\Omega)^n. \quad (1)$$

The dissolution rate is driven by a thermodynamic potential $(1-\Omega)$. A mineral's saturation state, Ω, is defined as the *in situ* calcium and carbonate ion concentrations divided by the apparent solubility product for that mineral ($[Ca^{2+}][CO_3^{2-}]/K'_{sp}$). Undersaturation is related to the dissolution rate by a rate constant, k, and a reaction "order", n. This reaction order is of ambiguous significance; in this case it solely describes empirical relationship between the saturation state and the dissolution rate. Global modeling efforts have focused on a linear ($n = 1$) formulation, since it is relatively easy to implement (Hales and Emerson, 1997b; Dunne et al., 2012; Ilyina and Zeebe, 2012; Boudreau, 2013). However, many experimental and *in situ* studies suggest nonlinear relationships between undersaturation and dissolution rate (Berner and Morse, 1974; Honjo and Erez, 1978; Keir, 1980; Cubillas et al., 2005; Gehlen et al., 2005b; Berelson et al., 2007; Fukuhara et al., 2008). In one of the most influential studies, Keir (1980) found carbonate dissolution kinetics in seawater to be both very nonlinear and very fast ($n = 4.5$, $k = 1300\%$/day). Kier's experimental dissolution rate is about an order of magnitude faster than those determined *in situ* (Honjo and Erez, 1978). In fact, almost all laboratory dissolution studies outpace rates determined in the water column.

While a few other dissolution rate studies have been performed in natural seawater (Morse and Berner, 1972; Gehlen et al., 2005b), the applicability of many dissolution rate determinations to oceanographic conditions is extremely limited, due to solution chemistry and distance from equilibrium. For instance, most of the mechanistic work performed on calcite is far from equilibrium in dilute or non-seawater solutions (MacInnis and Brantley, 1992; Arakaki and Mucci, 1995; Shiraki et al., 2000; Fischer et al., 2012 and references therein). Moreover, mechanistic studies are typically performed on a small area on individual grain surfaces, while the oceans interact with entire, complex particles. Thus, the real quantity of interest is a bulk dissolution rate. The disagreement among laboratory determinations, and the large discrepancy between lab and *in situ* results, lead to limited understanding of the dissolution process, and uncertainties in the implementation of a dissolution rate law in earth system models and projections.

Here, we present novel measurements of calcium carbonate dissolution that rely on a closed system dissolution measurement. We perform these experiments in natural seawater close to equilibrium, capturing the range of undersaturations experienced by carbonates in the ocean. Using our new method, we are able to completely constrain and maintain experimental saturation state, and also maintain near-constant surface area throughout the experiment. Our bulk dissolution study thus represents a potential link to detailed, mechanistic studies of solid-solution interfaces.

2. MATERIALS AND METHODS

Our method takes advantage of high precision stable isotope ratio measurements on a Picarro cavity ringdown spectrometer (CRDS). We use the stable isotope of carbon, ^{13}C, as a direct tracer of mass transfer from mineral to solution. In general, calcium carbonates enriched in ^{13}C are placed in a closed system of undersaturated seawater. We then sample the evolving $\delta^{13}C$ of this seawater over time, obtaining curves of moles dissolved over time. The slope of these curves is a direct measure of mass loss rate from the mineral. First, we present the synthesis and characterization of the materials used in this study. Second, we describe our measurements of the carbonate system during an experiment – dissolved inorganic carbon (DIC), and total alkalinity (TA) – and the subsequent calculation of experimental saturation state. Finally, we describe the setup and execution of our dissolution rate experiments, $\delta^{13}C$ measurement, data fitting techniques, and analysis of uncertainty.

2.1. Labeled calcium carbonates

Calcium carbonates enriched in ^{13}C are not produced naturally. Therefore, all of the materials used in this study were either purchased or prepared in the laboratory. We confirmed mineralogy with XRD and/or Raman spectroscopy, and measured specific surface area using either Nitrogen, Argon, or Krypton adsorption isotherms, fitting

the curves following the BET method (Brunauer et al., 1938). SEM imagery was also obtained, using a Hitachi TM-1000 environmental SEM. Mineralogical determinations with XRD and Raman spectroscopy both have detection limits of ~1% for calcium carbonate polymorphs (calcite, aragonite, and vaterite; Kontoyannis and Vagenas (2000)). Thus, we are confident in our mineralogies to ~99% purity.

Synthetic $Ca^{13}CO_3$ was purchased from Sigma Aldrich (SKU 492027, ⩾99 atom%). In all experiments performed with Aldrich calcite, this stock powder was wet-sieved to a grain size of 70–100 μm using 18.2 MΩ water adjusted to a pH of ~8 using ammonium hydroxide.

The above material, while inexpensive and plentiful, is not ideal due to its sintered nature. We also needed a well-formed material that can be manipulated as an inorganic solid in a range of grain sizes. To this end, we grew our own calcium carbonates in the laboratory, using a gel-diffusion method first described by Nickl and Henisch (1969). In this method, a 120 mL glass U-shaped tube was filled with 50 mL hydrous gel (0.17 M sodium metasilicate, adjusted to pH 8), separating 30 mL reservoirs of $CaCl_2$ and $Na_2^{13}CO_3$ (both 0.15 M) in each arm of the tube. The ends of the tube were sealed using Parafilm and rubber stoppers. Nucleation of calcium carbonate crystals was limited by diffusion and the gel pore spacing, allowing for slow growth of large grains. Grains were harvested after 3–6 months of reaction time by pouring off the spent reservoir solutions followed by physical break-up, sonication, and decantation of the less dense gel matrix from the calcium carbonate grains. Grains were then triply washed in DDW and dried at 60 °C. In this study, we present data from Aldrich-supplied and gel-grown calcite, dry-sieved to several size fractions. The degree of isotopic labeling was measured using a Picarro CRDS on small (0.2 mg) aliquots of material, pre-acidified, and introduced to the Picarro using the AutoMate Liaison autosampler. Raw isotopic abundances were used, and compared against a standard curve, prepared by sequentially diluting fine-sieved pure ^{13}C Aldrich calcite into natural abundance optical calcite.

2.2. Surface area determination

Surface areas were determined using two different methods. First, the specific geometric surface area of the calcites were calculated using the mean sieving size and assuming cubic geometry:

$$S.A._{geom} = \frac{6}{\rho \cdot \bar{d}}; \quad (2)$$

where $\rho = 2.63$ g/cm^3 is the assumed density of calcite and $\bar{d}$ is the mean grain diameter of the sieved fraction. Secondly, "total" specific surface areas were determined by the BET method (Brunauer et al., 1938), using Ar, N_2, and/or Kr gases. Raw data (pressure (p), reference pressure (p_0), and volume (V)) were plotted as $\frac{p}{V(p-p_0)}$ vs $\frac{p}{p_0}$, in the linear region of $0.04 < p < 0.5$, fitted using a linear regression, and the surface area was calculated as in Brunauer et al. (1938) These regressions typically gave relative errors of 1–3%.

2.3. Carbonate system parameters

We constrained calcite saturation state using DIC-TA pairs. All of our experiments were performed in Dickson seawater reference material (poisoned with mercuric chloride, final concentration ~0.0015% by weight or 55 μM). The phosphate concentrations in all Dickson batches used were between 0.55 and 0.58 μmol/kg. We first made up large batches of undersaturated water for use in dissolution experiments. About 2–3 L of Dickson seawater standard was siphoned to 5 L Supelco gastight foil bags (Part no. 30228-U). Undersaturation was achieved by titrating alkalinity via injection of HCl (0.1 M) through the sampling port septum of the foil bag. No DIC was lost during acid addition. DIC did change slightly, but only due to dilution by the added HCl solution. These reservoirs could be used for 6–10 experiments, allowing for replicate experiments at the same degree of undersaturation.

Alkalinity, determined by open-system Gran titration, was performed on a custom-built instrument. We used a Metrohm Ecotrode (part no. 6.0262.100) electrode connected to a Mettler Toledo SevenCompact pH meter. The titrant (0.05–0.1 M HCl in natural seawater) was delivered by a Metrohm 876 Dosimat Plus titrator with a 5 mL burette. Titrant concentration was determined by calibration to seawater standard reference materials. To run a sample, ~16 mL of seawater was filtered and weighed into a plastic sample container, which was placed into a 21.0 ±0.1 °C water bath. The sample was stirred with a Teflon-coated stir bar and bubbled with air throughout the measurement. The titration was controlled from a Windows laptop using a home-coded MATLAB script. Initial acid injection and stabilization took about 5 min; then, the titration dosed 0.01 mL of acid and measured pH in 20 s intervals. After a total of 12 time points, alkalinity was determined using a nonlinear least-squares approach as outlined in the Best Practices guide (Dickson, 2009). Dickson standard reference materials, as well as an in-house seawater alkalinity standard, were run at the beginning and end of every session to ensure analytical consistency and to monitor acid and electrode drift. Long-term alkalinity precision is about 2.0 μeq/kg (1σ, Fig. 1) over several months, based on our internal standard. There is also a slight decrease in replicate standard deviation over this measurement period; this mainly represents the increasing experience of the analyst, rather than a true decrease in the variance of the standard. Long-term accuracy is about the same as precision; thus total alkalinity error over the long-term is on the order of 2 μmol/kg (Table 1).

Dissolved Inorganic Carbon (DIC) and seawater $\delta^{13}C$ were determined using a Picarro CRDS (G2131-i) coupled to Picarro Liaison interface and a modified AutoMate autosampler. About 7 mL of filtered seawater was injected into an evacuated, pre-weighed, 12 mL AutoMate vial from a syringe through the rubber septum screw-cap. The net sample weight was recorded. The AutoMate acidified these samples on-line using 10% phosphoric acid, and the resulting CO_2 was carried in a nitrogen stream, through a Nafion desolvating line, to the Picarro Liaison sampling bags. The flow of gas from the AutoMate into the Picarro Liaison's

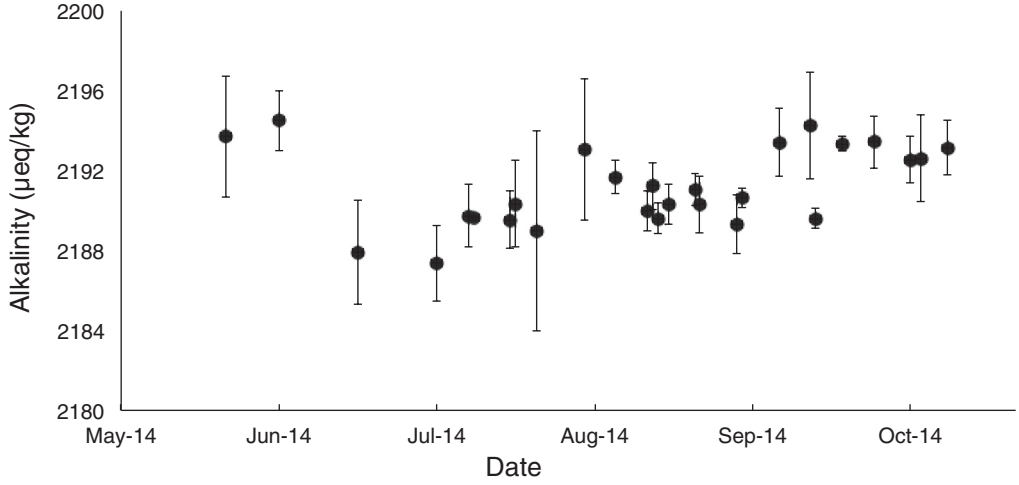

Fig. 1. Long-term precision and drift of our in-house alkalinity standard. Data points are the mean of the standard replicates collected during the analytical session that day; error bars are the 1σ standard deviation of the replicates.

Table 1
Error analysis of Alkalinity, DIC, and Ω in this study. Internal errors are due to the goodness of data fit and precision of mass flow for Alkalinity and DIC, respectively. Intermediate errors are the standard deviation of replicates run in a single analytical session. External errors are the standard deviation of replicates run over multiple analytical sessions. Note the similarity between all of these values, indicating that errors are traceable to the initial measurement error.

	Alkalkinity (µeq/kg)	DIC (µmol/kg)	Ω
Mean value	1960–2200	~ 2000	0.6–3.0
Internal error (1σ)	2.5	5.1	–
Intermediate error (1σ)	2.0	5.6	–
External error (1σ)	2.0	5.2	0.01–0.025

discrete sample bag was mass flow controlled such that every bag had precisely the same mass of N_2+ CO_2. Each bag was then introduced to the Picarro CRDS for continuous analysis over an 8 min interval.

Averaging statistics on each of these sample peaks were taken to give final CO_2 concentrations and isotopic compositions. Drift in both DIC and $\delta^{13}C$ was monitored over the course of the run, and also over longer time periods. DIC values were normalized to reference material values, and samples were both blank-and standard-corrected. Since we do not care about absolute $\delta^{13}C$ values, only relative changes, and because there are no available seawater $\delta^{13}C$ reference materials, standard $\delta^{13}C$ values were normalized to an arbitrary value of 1‰ (VPDB). Samples were corrected for instrumental drift using linear interpolation between bracketing standards (at the beginning, middle and end of the run, typically 7–10 h). We also have documented a negative correlation between water content and $[^{12}CO_2]$ (and thus $\delta^{13}C$). Although most water is removed via Nafion reverse flow partitioning, we monitored water content in our samples, and made a water correction if necessary. Drift over the course of a run (~10 h) was almost never above a few tenths of a permil, and resulting Picarro standards (Dickson standard seawater) typically had a standard deviation of under 0.1‰. The error in our DIC values can be entirely traced to fluctuations in flow rate: the standard deviation of replicate seawater samples has a relative error of 0.2/80 standard cubic centimeters per minute (SCCM), or ~5.1 µmol/kg (Table 1). We were able to take advantage of replicate DIC and Alkalinity analyses to use standard errors when calculating experimental Ω and its uncertainty.

Alkalinity and DIC pairs were then converted to saturation state using CO2SYS (v1.1, 2011) run through MATLAB. We used the acid dissociation constants of Dickson and Millero (1987). The errors in Alkalinity and DIC were propagated to $\Omega_{calcite}$ by a Monte Carlo approach: Alk-DIC pairs were sampled randomly from normal distributions with their associated standard errors as the standard deviations, and the resulting Ω values were averaged. Errors on Ω, calculated this way, were between 0.01 and 0.04 units. The calcite solubility data from Mucci (1983) were used for calculation of Ω in CO2SYS. We later discuss the experimental evidence in support of Mucci (1983) solubilities.

2.4. Dissolution rate experiments

All dissolution rate experiments presented here were performed on the benchtop at ambient temperature (20 – 22 °C). Prior to experimentation, we evaluated several different materials for their effect on DIC and alkalinity to construct our experimental apparatus, since we needed excellent control on saturation state.

2.4.1. Unacceptable materials

Our first experiments were performed in Tedlar bags, which proved permeable to CO_2. In Tedlar, udersaturated seawater with a pCO_2 of over 2000 ppm lost an average of 1 μmol/kg DIC per day over a 10-day period. We then switched to Supelco inert foil bags, which demonstrated a stable DIC and did not add or remove alkalinity. Secondly, we needed a material that would retain our labeled carbonate grains during an incubation experiment. We initially sealed our grains in Nylon mesh bags. However, we found that this amide polymer slowly increased the alkalinity of the experimental seawater over time. No amount of washing or pre-conditioning changed this alkalinity increase. Additionally, as our mesh bags were constantly moving and bending, this alkalinity increase did not happen all at once, but slowly over time, by 10–15 μeq/kg over 5 days (Fig. 2). Heat-sealing the Nylon – crucial for retaining grains – further increased alkalinity contamination. presumably due to disintegration of the Nylon polymer.

Instead of sealing grains in Nylon mesh, we placed grains directly into the foil bag and used specially fabricated polycarbonate sampling ports. These ports have a built-in filter housing, such that sampled water is filtered through Nuclepore membrane filters (~0.2 μm, Fig. 3). The port was fitted onto the bag through a punched hole, hand-tightened, and sealed with a Viton o-ring. Using this setup, both alkalinity and DIC blank experiments showed no change over days to weeks.

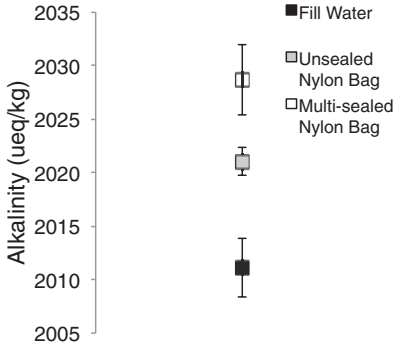

Fig. 2. Documented alkalinity increase in a Supeclo inert foil bag over 5 days with (black symbol) no Nylon mesh, (gray symbol) unsealed Nylon mesh, and (open symbol) multiply-sealed Nylon mesh.

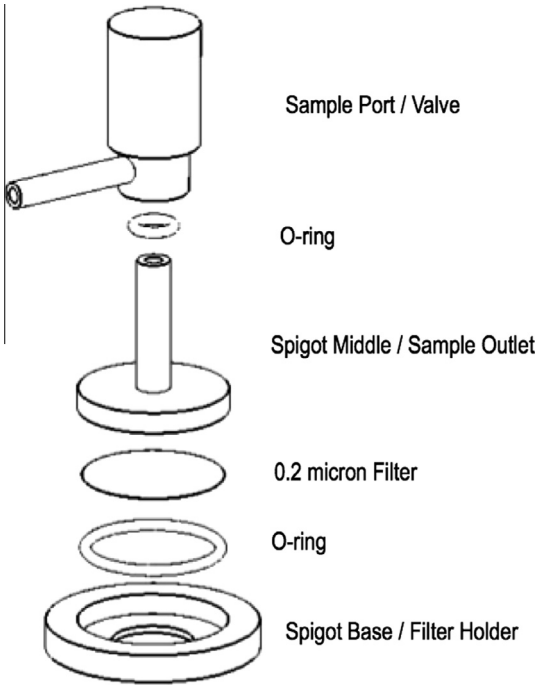

Fig. 3. A diagram of the custom-made sampling port used in our experiments. Filter is an 0.2 μm Nuclepore membrane filter. The foil bag wall sits between the sample port and spigot middle, sealed by a Viton o-ring.

2.4.2. Experimental setup

Experiments were prepared in the following way: 1 L Supelco bags (part no. 30336-U) were cut open, and the sampling ports were fitted through the foil. Labeled material (3–5 mg) was weighed out and quantitatively poured into the foil bag. The open bag was then heat-sealed shut, twice, creating a double seam. These bags were then evacuated to remove all headspace. Undersaturated fill water was siphoned from the large foil reservoirs into these experimental bags. First, about 50 g was siphoned in, and grains were agitated and rinsed. This water was then removed through the sampling port via syringe and discarded. Then, about 300 g of fill water was siphoned in, the bag was weighed to obtain the exact mass of water added, and the experiment was considered started once the bags were placed on a shaker table at 60 rpm. We have tested the shaking rate and found that at speeds above 60 rpm, the dissolution rate is the same as the rate at 60 rpm. Below 60 rpm, rates slowed significantly, presumably due to stagnation and the formation of boundary layers around the grains. At each sampling point, the experimental bags were weighed. Samples were withdrawn through the sampling port via a Tygon tube attached to a plastic syringe. The syringe was washed with about 2 mL of sample water, and then a full 7 mL sample was taken, carefully avoiding headspace. This sample was injected through a 0.45 μm filter into a pre-evacuated, pre-weighted AutoMate vial for Picarro analysis. Initially, sampling occurred either 2 or 3 times daily. As the experiment proceeded, however, sampling became more infrequent. Total experiment duration lasted 6–12 samplings over 3–10 days. Since we measured DIC and $\delta^{13}C$ simultaneously, DIC was monitored over the course of the run. Post-experiment alkalinity measurements were also taken to check for alkalinity consistency.

2.4.3. Data processing

Data processing required manipulating the raw Picarro data to generate DIC and $\delta^{13}C$ values. Total CO_2 concentrations were blank-corrected (typically 15 ± 4 ppm in $\sim$ 1200 ppm), mass-normalized, and corrected using a multiplication factor determined by reference material standards run in the same analytical session. We converted $\delta^{13}C$ signals over time into a mass loss rate, or moles

dissolved over time. This is done by first converting $\delta^{13}C$ into moles dissolved. The $^{13}C/^{12}C$ ratio of seawater, R^{13}_{sw}, is related to $\delta^{13}C_{sw}$ by:

$$R^{13}_{sw} = (\delta^{13}C_{sw}/1000 + 1) \cdot R^{13}_{PDB}, \quad (3)$$

where R^{13}_{PDB} is the standard isotopic ratio of Pee Dee Belemnite (0.0112372). Assuming no addition of ^{12}C, the isotopic ratio change from sample to sample of the seawater was converted into a change in the moles of ^{13}C added to the solution, modified by the change in mass due to sampling:

$$\Delta^{13}C_{2-1} = m_1 \cdot [^{12}C]_{init} \cdot (R^{13}_2 - R^{13}_1), \quad (4)$$

where m_1 is the seawater mass of time point 1, $[^{12}C]_{init}$ is the initial ^{12}C concentration of the seawater in μmol/kg (which remains unchanged while dissolving 100% labeled materials) and R^{13}_i is the isotopic ratio measured at time point i. $\Delta^{13}C_{2-1}$ is then the change in moles of ^{13}C between time points 1 and 2. These incremental changes are cumulative, so that the total moles dissolved are summed over the time course. Typical dissolution experiments that use a carbonate mass of 5 mg and a bag volume of 300 mL yield a $\delta^{13}C$ change of about 20‰ for every 1 μeq/kg change in alkalinity in the reaction chamber. As an experiment proceeds and seawater is removed for sampling, a constant dissolution rate will have a larger impact on this smaller reservoir. Due to this diminishing reservoir effect, our sensitivity is closer to 10‰ per μeq/kg alkalinity change by the end of an experiment. When alkalinity changes were large, we used the mean bag alkalinity to calculate Ω, and used a standard deviation instead of standard error to calculate the error on Ω.

3. RESULTS

3.1. Solid characterization

The solid-phase carbonate minerals we use in our experiments, highly enriched in ^{13}C, come from two different sources: Aldrich and homegrown (Fig. 4). The composition of Aldrich calcite was confirmed to be 100% calcite via XRD. Aldrich calcite came as a fine powder which, upon closer inspection, was composed of sintered clumps of grains about 20 μm in diameter (Fig. 4)). Gel-grown calcium carbonate was formed in a range of grain sizes and morphologies; predominantly as well-formed rhombs. Additionally, a vaterite phase was formed in the shape of rough spherules of various sizes, as first observed by Schwartz et al. (1971). These two polymorphs were separated manually. The larger, homegrown rhombs were confirmed as 100±2% calcite by Raman spectroscopy. We also confirmed that these grains are 100% $Ca^{13}CO_3$ by measurement on the Picarro, as described above. Grain surfaces, however, revealed two distinct surface types. There were smooth, terraced features, as well as rough, poorly formed surfaces (Fig. 4f). Raman spectroscopy on both of these surfaces confirmed that, despite very different morphology, they were both calcite. As shown in Nickl and Henisch (1969), gel-grown grains retain some of the gel matrix during crystal growth. Thus, these differences in morphology could be guided by interaction with the gel matrix rather than any true mineralogical difference. Vaterite was present as separate crystalline units, so we cannot rule out that vaterite was present on our grains below our detection limit of ~ 1 – 2% compositional purity.

Various estimates of grain surface areas (Table 2) were compiled to compare methodologies. BET surface areas measured with N_2 and/or Argon are 2 to 3 orders of magnitude larger than corresponding geometric surface areas. Krypton has more promise as an adsorbate, as it has been demonstrated to give accurate surface areas down to 0.05 m^2 total area (de Kanel and Morse, 1979). We measured Kr-BET surface areas with different amounts of Aldrich calcite sieved to 70–100 μm, and found that the measured surface area is also strongly dependent on the sample size (Table 2). At lower sample sizes, the BET specific surface area is much larger. Measurements agree well within error at a single mass, while increasing sample size decreases the measured surface area to a threshold level of about 0.087 m^2/g for Aldrich calcite. We interpret the ~ 3x difference between geometric and Kr-BET areas as a measure of the surface roughness of the Aldrich calcite. We have chosen to normalize all of our dissolution rate data to geometric surface area because of inaccuracies in our N_2 and Ar BET data.

3.2. Dissolution experiments

The first step in converting raw $\delta^{13}C$ vs. time (Fig. 5a) to the number of moles dissolved is to fit straight lines and calculate the experiment's slope (Fig. 5b). This quantity is normalized to the mass of the solid used in each experiment. As shown in Fig. 5, there appears to be a change in slope at about 24 h. We use this second slope to calculate dissolution rates. The choice of using the second slope is discussed in Section 4.1. Slopes, intercepts, and the goodness of fits are obtained using the LINEST function in Microsoft Excel. *R*-squared values on these slopes range from 0.98 to 1.00. These linear regressions, while quite strong, are not as strong as those predicted from scatter on individual $\delta^{13}C$ measurements alone. Thus, the error in the fit here is indicative of not only instrumental precision, but experimental conditions as well.

We measured the alkalinity of the fill-waters and of the individual bags once an experiment finished. Samples for DIC are taken throughout the course of an experiment, so CO_2 loss is monitored. We find that after filling an experimental bag, DIC values are about 5–10 μmol/kg lower than the original fill water used. This DIC loss is attributed to CO_2 adsorption and diffusion into and through the tygon tubing used for solution transfer. Once the siphon is complete and the experiment underway, DIC loss is imperceptible given our measurement error (Fig. 5c). All pre-and post DIC and alkalinity values are presented in Table 3. The calculated saturation states from these Alk-DIC pairs are also presented, along with their Monte Carlo-estimated errors. Since we know quantitatively how many moles of carbon have been added to solution, we can calculate a final alkalinity change due to carbonate dissolution, and compare this to the measured alkalinity after an experiment is finished. We

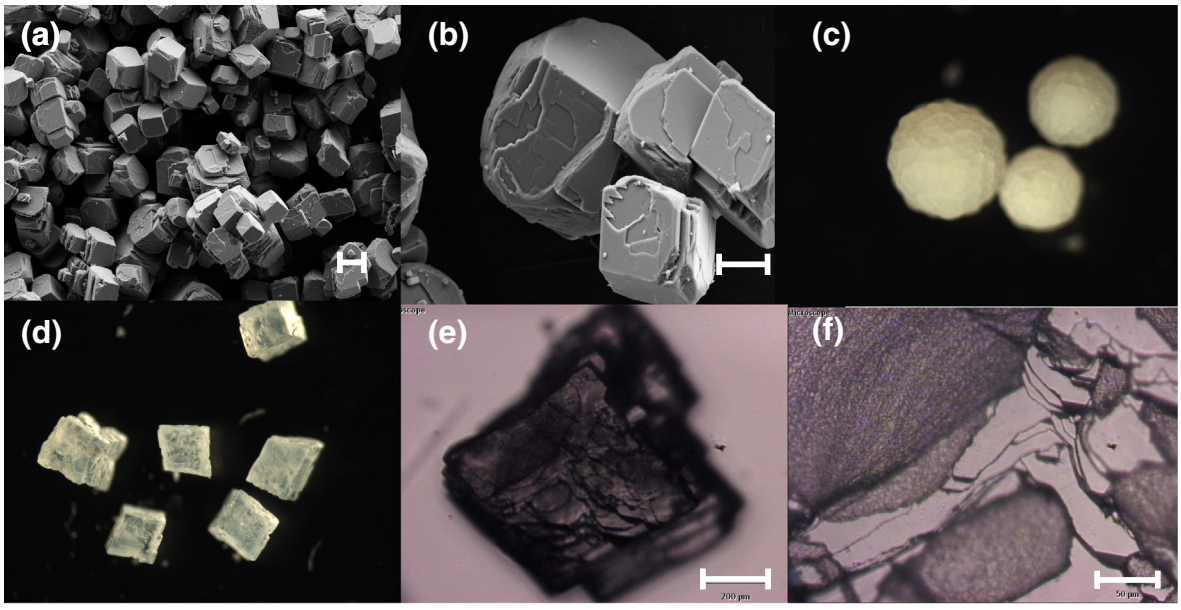

Fig. 4. Materials used in this study. (a and b) SEM images of the Aldrich ^{13}C-calcite, sieved to 70–100 µm. Notice the clumps of sintered grains, each about 20 µm in size. Scale bars are 20 and 10 µm, respectively. (c) Vaterite spherules at 6× magnification. Mineralogy confirmed by Raman spectroscopy. (d) Transmitted light micrographs of the homegrown calcite, sieved to 500–700 µm, at 6× magnification. (e and f) Reflected light micrographs of the same homegrown calcite grains. Notice the different textures, from a rough, sandpapery texture to smooth terraces. Both surfaces are confirmed to be calcite. Scale bars are 200 and 50 µm, respectively.

Table 2
A summary of the specific surface areas determined in this study. Method is either calculating a geometric surface area using Eq. (2) or determined through BET using argon, nitrogen, or krypton as the analysis gas. The mass refers to the amount of sample used in the BET determination.

Material	Mass (g)	Method	Surface area (m^2/g)	Error
Aldrich 70–100 µm		Eq. (2)	0.027	
	0.136	Ar-BET	4.514	0.126
	0.585	N_2-BET	0.536	0.013
	0.172	Kr-BET	0.150	0.015
	0.172	Kr-BET	0.136	0.013
	0.585	Kr-BET	0.095	0.006
	0.585	Kr-BET	0.090	0.004
	0.806	Kr-BET	0.085	0.004
	0.806	Kr-BET	0.089	0.005
Homegrown 300–500 µm		Eq. (2)	0.0057	
	0.085	Ar-BET	0.513	0.03
Homegrown 500–700 µm		Eq. (2)	0.0038	
	0.187	Ar-BET	7.65	0.23

use the final alkalinity value and experiment bag-DIC value to calculate saturation state, since the initial and final (calculated and measured) alkalinity values never differ more than 6 µeq/kg from each other. When the final and initial alkalinities differ by more than 5 µeq/kg, we use the average alkalinity in the bag over the course of the experiment, calculated using the changing bag mass and cumulative moles of carbonate ion added at each time point.

Saturation state as 1-Ω and dissolution rates are plotted against each other (Fig. 6). Data are fitted using a log-linear formulation of Eq. (1 and a log-linear regression which includes errors on both dissolution rate and Ω:

$$\log(\text{Rate}) = \log(k) + n \cdot \log(1 - \Omega), \quad (5)$$

where log(k), the intercept, is the logarithmic dissolution rate constant in g/g/day or g/cm^2/day, and n, the slope, is the reaction order. This form of linear regression was first described in the geochemical community by York (1966), and explicitly includes errors in the x-variable as well as the y-variable. These data are presented for Aldrich calcite

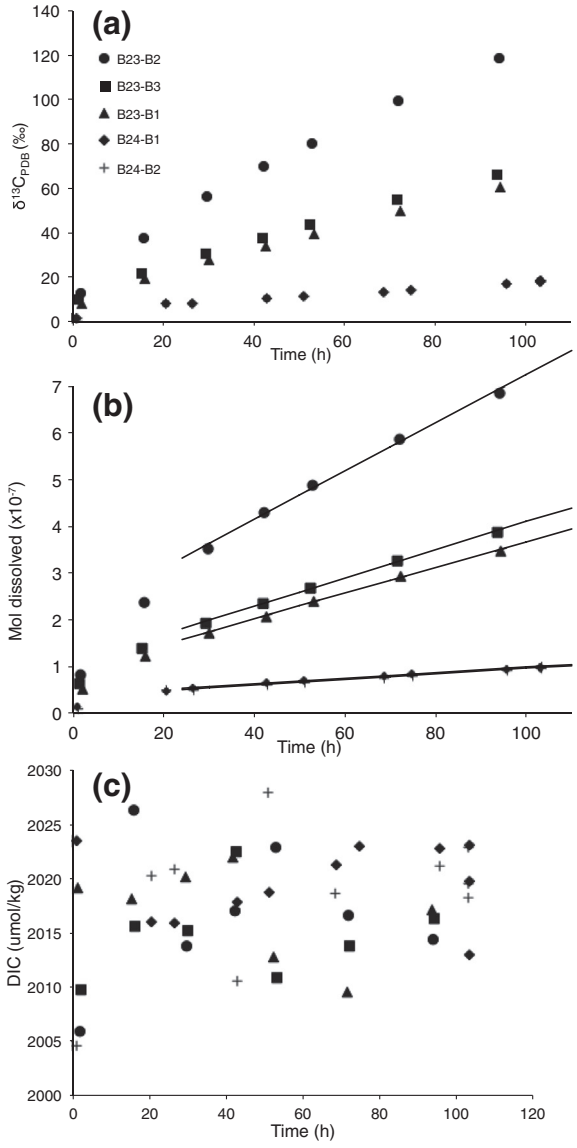

Fig. 5. Raw data from experiments B23 and B24. Each symbol type represents a single dissolution experiment, with discrete samples collected over the time displayed. Steeper slopes are measured in bags with greater undersaturation. (a) Raw isotopic CO_2 data. Each point is a single Picarro measurement of $\delta^{13}C$. (b) The data from (a) converted to the moles of labeled carbonate dissolved based on Eq. (4). Lines plotted are fits to the data after 24 h. (c) The DIC data over time for each experiment. Statistics on these data, rate calculations, and final undersaturations are presented in Table 3.

and two grain sizes of homegrown calcite, in Table 4 and Fig. 7.

4. DISCUSSION

4.1. Choice of thermodynamic constants

Accurate measurements of the carbonate system in seawater are dependent on the appropriate choice of thermodynamic constants, and calcite dissolution is no exception. We chose to use the Dickson and Millero (1987) refit of Mehrbach's data (Mehrbach et al., 1973) for the carbonate system dissociation constants. We also tested sensitivity to the choice of dissociation constants on calculation of Ω, and found that the use of constants from Lueker et al. (2000) change the calculated value of Ω by only as much as 0.002 units, well below the measurement error of Ω.

The other important constant is the K'_{sp} for calcite in seawater. If the calcite K'_{sp} value used in our study is too small, then a plot of dissolution rate versus undersaturation (1-Ω) will shift towards equilibrium, making it appear more linear. Hales and Emerson (1997b) recast the original dissolution data from Keir (1980) using updated carbonic acid dissociation constants and extrapolated to zero-dissolution to find a saturated ion activity product. These recalculations found dissolution rate to be essentially linearly dependent on undersaturation. Current estimates for a calcite solubility product by Gehlen et al. (2005a) are either the same as or larger than that of Mucci (1983) (the value used in our Ω calculations). Using the values of Gehlen et al. (2005a), our curves would shift towards higher undersaturation, rather than towards equilibrium. Furthermore, Gehlen et al. (2005b) show that their updated values of K'_{sp} also produce a nonlinear relationship in Keir's data. Finally, our own data indicate that the K'_{sp} Gehlen et al. (2005a) may be more accurate than that of Mucci (1983). In a long-term dissolution experiment of our Aldrich calcite, we measured DIC and alkalinity after about 2 months, and found that the carbonate ion concentration indicated an IAP for our Aldrich calcite to be 1–10% higher than that of Mucci (1983). We cannot give a more accurate estimate of the K'_{sp} for our calcite, since we suspect there might have been a small amount of DIC loss during this long-term incubation. Shorter-term solubility experiments using aragonite indicate that a larger solubility product is reached in under two months. We could choose to use a different "short-term" K'_{sp} that might be more appropriate for our day-to-week-long experiments, but it is difficult to determine if such a quantity would be truly a thermodynamically stable solubility product, or if there are still unbalanced kinetic processes occurring.

In order to further confirm our choice of K'_{sp}, we performed several short-term experiments in supersaturated seawater very close to equilibrium (Fig. 8). Experiments performed in 30% supersaturated seawater ($\Omega = 1.3$) showed no appreciable exchange over 10 days. A supersaturated experiment closer to equilibrium ($\Omega = 1.07$) shows definite isotopic enrichment over 7 days (Fig. 8b). This near-equilibrium ($\Omega = 1.07$) enrichment could be due to isotopic exchange, or it could be due to actual carbonate dissolution. Solid-solution exchange has been investigated before, and typically models partition the solid into labile and trapped reservoirs of calcium and carbonate groups on the calcite surface (Badillo-Almaraz and Ly, 2003; Tertre et al., 2010). Using radiolabeled calcium and bicarbonate, Tertre et al. (2010) showed immediate (minutes to hours) exchange of the labile solid surface with the solution; after this initial equilibrium was reached, the solid

Table 3
Carbonate system parameters and mass-normalized dissolution rates for all of the experiments presented in this study. Standard errors are accompanied by the number of replicates, in parentheses. Saturation state is calculated via Monte-Carlo error analysis of final (or average) alkalinity and *in situ* DIC pairs for each experiment (see text for more details; n.c. = not collected).

Material	Expt.	DIC		Alkalinity				Ω		Rate	
		in situ (μmol/kg)	s.e. (1σ)	initial (μeq/kg)	Final, calc. (μeq/kg)	final,meas. (μeq/kg)	s.e. (1σ)	calc.	Error (1σ)	$\cdot 10^{-3}$ (g/g/day)	Error
Aldrich	B20-B1a	2026	1 (10)	1984	1985	1982	1 (4)	0.75	0.01	0.450	0.028
70–100 μm	B20-B1b	2018	2 (10)	1984	1986	1982	1 (4)	0.81	0.02	0.192	0.014
	B20-B2	2023	1 (20)	2004	2005	2002	1 (4)	0.90	0.01	0.048	0.004
	B22-B1	2011	2 (12)	1986	1987	1986	1 (3)	0.85	0.01	0.947	0.005
	B22-B2	2016	2 (12)	1987	1989	1991	2 (4)	0.83	0.01	0.215	0.009
	B23-B1	2017	2 (6)	1963	1966	1965	1 (4)	0.68	0.01	1.757	0.063
	B23-B2	2017	2 (5)	1957	1963	1963	2 (4)	0.66	0.01	3.935	0.304
	B23-B3	2016	2 (5)	1962	1968	1968	1 (3)	0.69	0.01	1.793	0.088
	B23-B4	2013	1 (5)	1973	1974	1973	0.2 (3)	0.75	0.01	0.549	0.078
	B24-B1	2020	2 (8)	1985	1986	1986	1 (4)	0.79	0.01	0.327	0.012
	B24-B2	2020	1 (9)	1985	1986	1988	0.3 (4)	0.81	0.01	0.367	0.005
	B30-B4	2027	3 (3)	2004	2005	2008	1 (3)	0.87	0.02	0.074	0.002
Low Ω	B35-B1	1967	5 (6)	939	999	983	21	0.017	0.001	87.51	4.47
	B36-B1	2051	4 (6)	1660	1680	1674	6	0.127	0.003	31.02	1.25
High Ω	B31-B1	2013	7 (4)	2046	2046	2046	0.1 (3)	1.33	0.06	N/A	N/A
	B31-B2	2022	2 (4)	2046	2046	2045	1 (3)	1.26	0.02	N/A	N/A
	B31-B3	2020	4 (4)	2054	2054	2055	1 (3)	1.27	0.04	N/A	N/A
	P13	2018	1 (10)	2022	2022	2022	1 (3)	1.07	0.02	0.017	0.002
Homegrown	B27-B1	2009	4 (6)	1971	1972	1974	1 (4)	0.78	0.02	0.147	0.010
300–500 μm	B27-B2	2020	2(5)	1995	1995	1993	1 (3)	0.84	0.02	0.068	0.007
	B27-B3	2017	3 (6)	1987	1988	1987	1 (4)	0.82	0.02	0.089	0.011
	B27-B4	2020	4 (6)	1977	1978	1976	0.2 (3)	0.74	0.02	0.310	0.036
Homegrown	B26-B1	2025	3 (7)	1985	1985	1989	1 (4)	0.76	0.01	0.127	0.007
500–700 μm	B26-B2	2018	4 (7)	1963	1964	1968	1 (3)	0.70	0.02	0.344	0.013
	B26-B3	2020	3 (7)	1957	1959	1960	1 (4)	0.64	0.02	0.629	0.016
	B26-B4	2012	1 (5)	1962	1964	n.c.	n.c.	0.70	0.01	0.516	0.015
	B26-B5	2022	1 (5)	1973	1974	1977	1 (4)	0.70	0.01	0.205	0.005

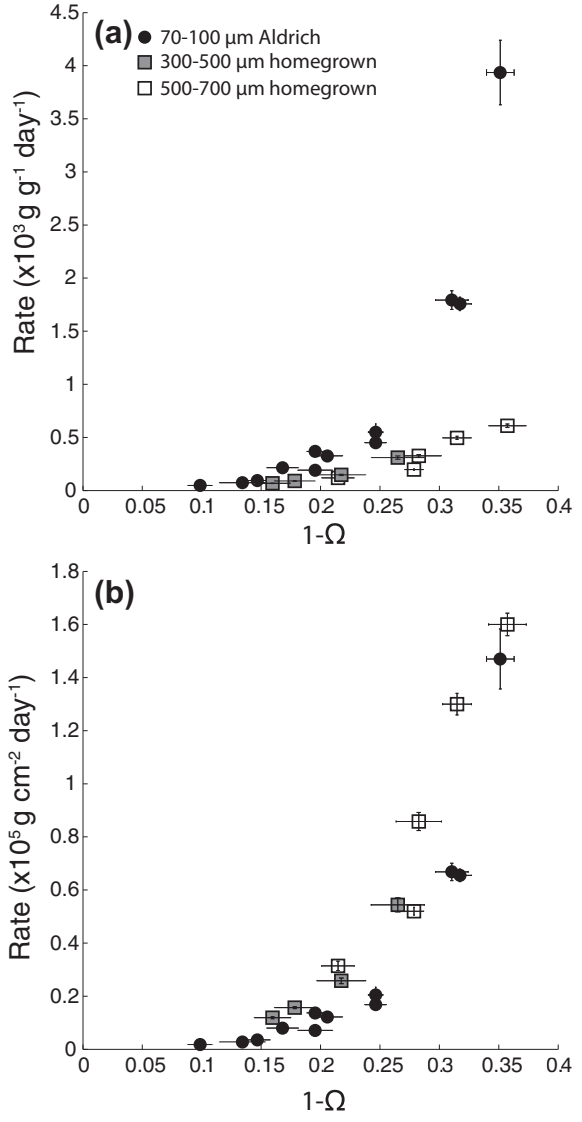

Fig. 6. Dissolution rates versus undersaturation (1-Ω) for Aldrich and homegrown materials. (a) Rates normalized to mass of carbonate. (b) Rates normalized to mass and specific geometric surface area. Note the rate unit and scale differences. Solid circles: 700–100 µm Aldrich calcite. Gray squares: 300–500 µm homegrown calcite. Open squares: 500–700 µm homegrown calcite.

maintained equilibrium for up to 10 days. Thus, exchange on the multi-day timescale is an unlikely contributor to our observed isotopic increases. We can confirm this hypothesis using a simple geometric calculation. If we assume a calcite mass of 5 mg in an experiment, and a surface area of 0.09 m^2/g, this gives a total surface area of $4.5 \cdot 10^{-4}$ m^2 of calcite per experiment. Next, if we assume that a unit cell of calcite is 0.5 nm deep, this gives a total volume of $2.25 \cdot 10^{-13}$ m^3, or $6.7 \cdot 10^{-9}$ mol in a monolayer on the total calcite surface. A 300 g seawater solution contains about $6 \cdot 10^{-4}$ mol DIC. If all of this surface monolayer were to exchange with seawater, this would lead to an isotopic increase of 1 part in $\sim 10^5$, or 0.01‰. This is a negligible increase in $\delta^{13}C$ relative to our measurement precision. On the other hand, if this enrichment is indeed dissolution, we would need to adjust our Ω by choosing a new K'_{sp} (see discussion below). The calculated dissolution rate of this experiment (Table 3) is about 35% of the dissolution rate at $\Omega = 0.90$. Assuming that the entire isotopic signal in this experiment is due to exchange, this would also be the maximum contribution of exchange to any of our reported dissolution rates. Our own determinations of K'_{sp}, in addition to the arguments against exchange made here, strongly support this near-equilibrium behavior being dissolution. We do not have direct measurements of K'_{sp} for our homegrown calcite. In order to be consistent across our two materials in this study, we do all calculations of dissolution parameters using the K'_{sp} estimate from Mucci (1983), and discuss this very near equilibrium dissolution data in the context of potential mechanisms of dissolution.

4.2. Surface area corrections

In all of our experiments, there are two stages of $\delta^{13}C$ accumulation in the bags (Fig. 5). In the first 24 h, rates are faster than thereafter. Following the first 24 h, rates remain constant over several days. There are several explanations for this increased initial rate. First, since our detection limits in determining mineralogy are at best 1%, this initial rate could be due to dissolution of a more soluble or hydrated calcium carbonate polymorph on the mineral surface. Secondly, this increased rate could reflect the mineral surface reaching steady state with the solution composition. These effects could be substantial, since calcium carbonates in all cases were precipitated from pure calcium

Table 4
Each material's rate law parameters in this study. Geometric surface areas calculated using Eq. (2). Errors (1σ) are calculated from a York regression accounting for errors in both rate and undersaturation.

Material	$\log k_{geom}$ (g cm^{-2} day^{-1})	k_{geom} (g cm^{-2} day^{-1})	n
Aldrich calcite 70–100 µm	-3.4 ± 0.1	$3.7 \pm 0.4 \cdot 10^{-4}$	3.5 ± 0.2
Homegrown calcite 300–500 µm	-3.6 ± 0.4	$2.4 \pm 0.9 \cdot 10^{-4}$	2.9 ± 0.5
Homegrown calcite 500–700 µm	-3.0 ± 0.3	$1.0 \pm 0.3 \cdot 10^{-3}$	4.0 ± 0.6
All inorganic data	-3.1 ± 0.1	$7.2 \pm 0.6 \cdot 10^{-4}$	3.9 ± 0.1

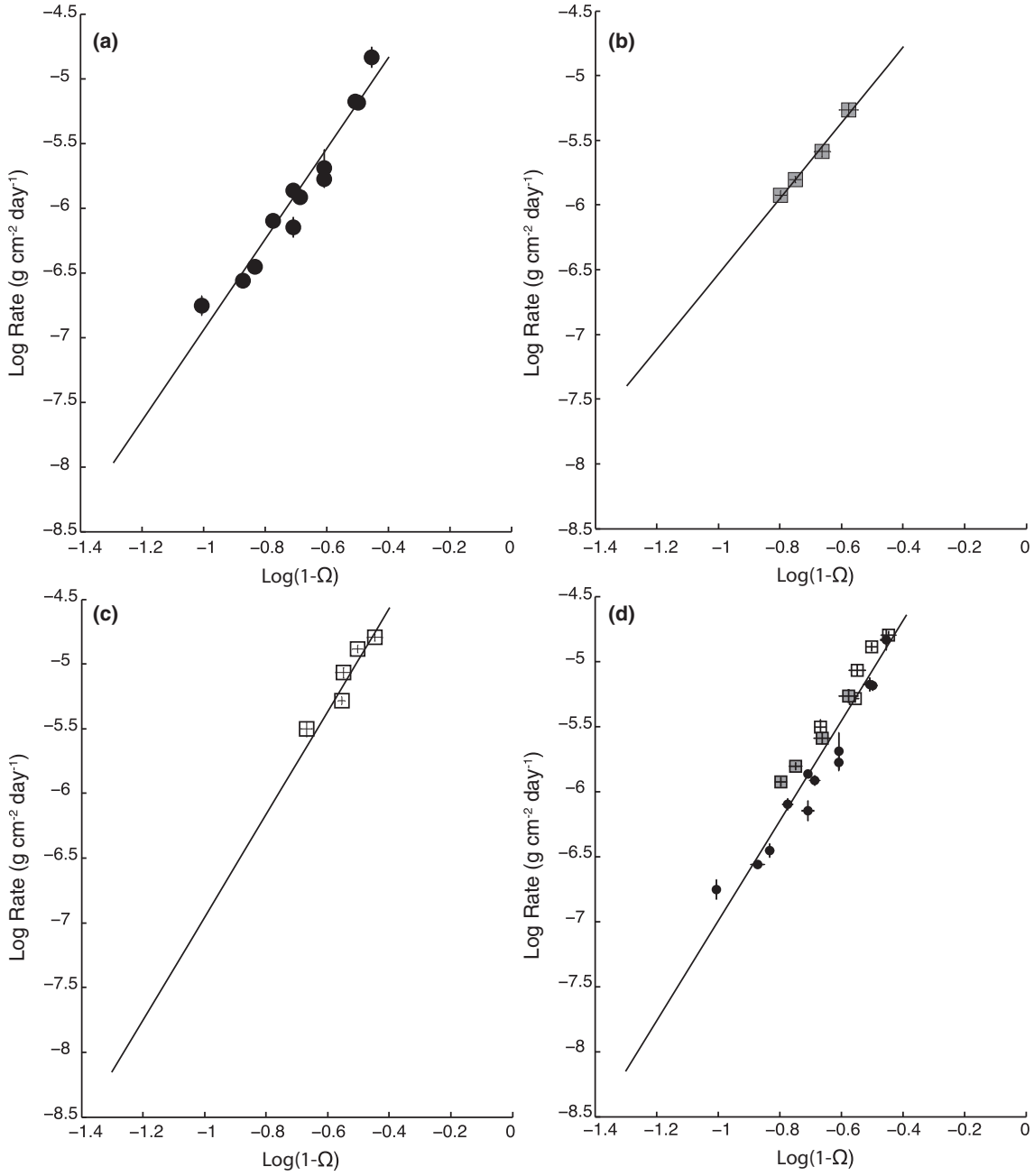

Fig. 7. Log–log plots of undersaturation versus geometry-normalized rate data for all materials presented. (a) 70–100 μm Aldrich calcite. (b) 300–500 μm homegrown calcite. (c) 500–700 μm homegrown calcite. (d) Geometry-normalized rate data for all minerals, fit as an ensemble. Symbols are the same as in Fig. 6. Slopes (log k) and intercepts (n) for these fits, along with the accompanying error analysis, are presented in Table 4.

chloride solutions. Thus, the calcite surface could be equilibrating with seawater Mg/Ca; it could be hydrating to adjust its water activity; and it could be adsorbing species such as dissolved organic carbon or phosphate ion. Finally, although we rinsed our grains with pH-adjusted DIW, these increased rates could be due to dissolution of fine-grained material and/or desorption of loosely bound carbonate ions from the mineral surface. We did not systematically test these various hypotheses, and we choose the later rates as representing the bulk crystal dissolution rates. We choose 24 h as an arbitrary cutoff between these slopes, since this effect never lasted longer than one full day. In no experiment was this period long enough to significantly change the experimental saturation state.

The fact that we see no further change in slope indicates that these are bulk dissolution rates, and that our system is remaining closed to any alkalinity or DIC change. Based on the number of moles dissolved at the end of our experiments, a maximum of 2% of the solid is consumed over the duration of an experiment. In most cases, $< 1\%$

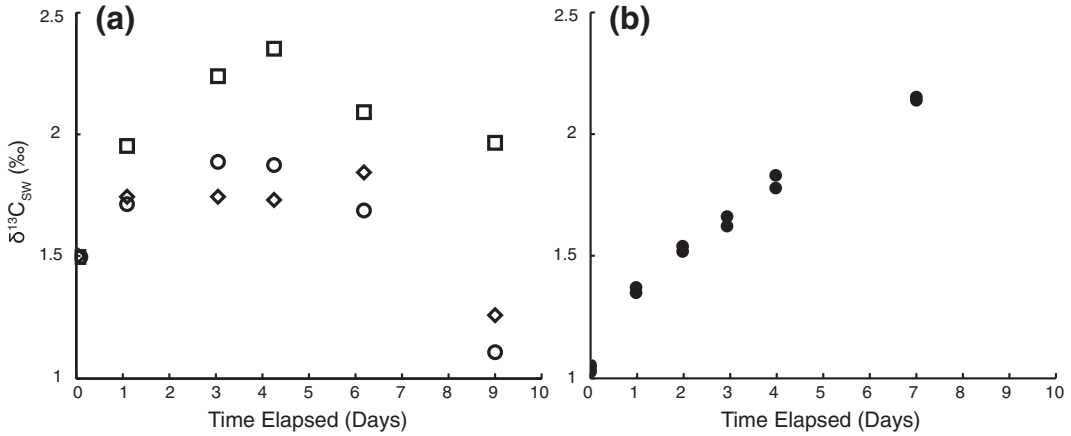

Fig. 8. Seawater isotopic data versus time for four experiments conducted at supersaturation ($\Omega \sim 1.3$) to test for isotopic exchange between solid and solution. (a) Three experiments conducted at $\Omega \sim 1.3$. These experiments show no significant isotopic enrichment over time. Each symbol type is an individual dissolution experiment. (b) One dissolution experiment conducted at $\Omega = 1.07$. There is some isotopic enrichment over 7 days.

dissolves. As above, there are $6.7 \cdot 10^{-9}$ mol in a monolayer on the calcite surface in our experiments. A 40‰ solution enrichment – $\sim 2 \cdot 10^{-7}$ moles of carbonate dissolved – corresponds to about 30 monolayers of calcite dissolved, or a 15 nm change in surface height. This surface height is consistent with surface height changes measured in AFM studies of calcite dissolutions (Tang et al., 2004; Arvidson and Lüttge, 2010) and are on the order of AFM tip sizes used in these experiments (4–50 nm; Teng (2004)). Thus, changes in surface area in our experiments are no greater than those observed in surface-based dissolution studies, and we can treat the surface area as constant throughout an experiment. Our tight control of surface area and bulk chemistry bridges the gap between detailed surface examinations of calcite dissolution, and bulk mineral dissolution studies.

Compiling the rate data (per gram) as a function of undersaturation (Fig. 6a) shows differences between the grains used in our experiments. As expected from an inverse-diameter relationship, the larger-grained material dissolves more slowly per gram than the Aldrich calcite. Indeed, when the data are normalized to geometric surface area, they collapse to a single curve (Figs. 6b and 7d). This agreement could be coincidental, due to the differences observed in surface morphology. It is also not unprecedented for different materials to have different dissolution rate constants (e.g. Carrara marble and Iceland spar; Sjöberg and Rickard (1984)). Data plotted in log–log space (Fig. 7d) indicate a slight offset between our homegrown calcites and the Aldrich grains. This offset could be due to differences in grain surfaces and crystal microstructure that are not captured by our geometry normalization, or small differences between the K'_{sp} of the two materials. The empirical fits also provide slightly different k and n values (Table 4 discussed below). The fact that our geometry normalization works across three grain sizes and two material types indicates that grain size plays a role in controlling dissolution rate. Since grain size correction alone normalizes our data quite well, it seems that the microstructural differences we observe are not of primary importance for dissolution rate.

We present data normalized by geometric, not BET, surface area (Table 4, Figs. 6–9). The BET method accounts for surface roughness and heterogeneity, whereas geometric normalization simply treats grains using an average grain size and a model grain shape (in our case a cube). For Aldrich calcite, our Kr BET result provides a maximum surface roughness that increases surface area over the

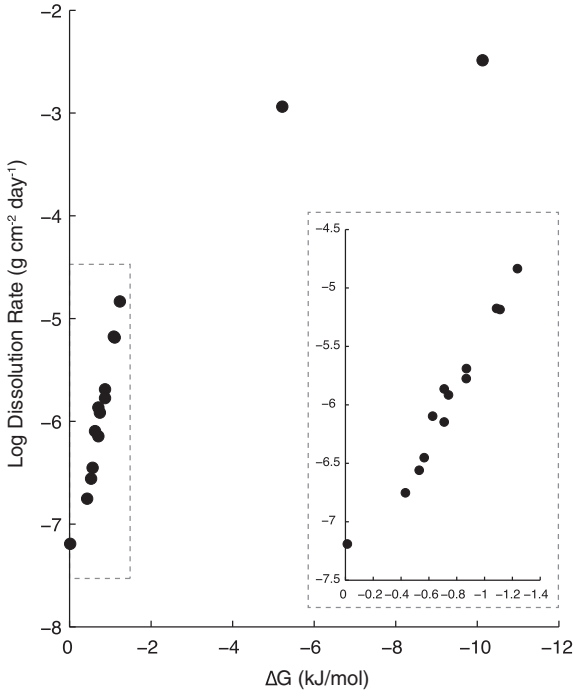

Fig. 9. Aldrich calcite dissolution rate data versus $\Delta G = RT\ln(\Omega)$. The lower right inset plots the very near-equilibrium data, illustrating curvature both near and far from equilibrium.

geometric estimate by a factor of ~3. We lack sufficient sample to analyze our homegrown material's surface area using Kr-BET. Normalizing to geometric surface area means the absolute dissolution rates presented in this study could be systematically high by a factor of 3. This is a large source of uncertainty for small quantities of materials. The use of geometric surface area is not unprecedented (Plummer and Wigley, 1976; Sjöberg, 1976; Sjöberg and Rickard, 1985; Shiraki et al., 2000; Cubillas et al., 2005), and with the exception of Keir (1980) and Honjo and Erez (1978), we restrict any quantitative rate comparison to other studies which normalized to geometric surface area.

4.3. The nonlinearity of calcite dissolution in seawater

Several arguments have been made for a linear relationship between dissolution rate and saturation state in seawater (Hales and Emerson, 1997b; Emerson and Bender, 1981; Boudreau, 2013). A majority of these studies have either been modeling attempts or refits of older experimental data (specifically from Keir (1980) and Keir (1983)). The first argument against a linear fit to our data is statistical. Fitting our data with a linear regression gives a poor r-squared value (0.72, not shown), and a significant negative *y*-intercept. A negative intercept would imply a large quantity of more soluble calcium carbonate, but none were detected given the detection limits of our methods (see above). Thus, a negative intercept must imply a large shift of calcite solubility towards numbers smaller than those determined by Morse et al. (1980), for which there has been no recent experimental evidence. In contrast to model fits of deep-sea sediments, most laboratory calcite dissolution data shows a strongly nonlinear dissolution rate, dating from as early as 1972 (Morse and Berner, 1972; Keir, 1980; Teng, 2004; Gehlen et al., 2005b; Xu et al., 2012). This nonlinearity is also not unique to calcite: similar results have been shown for near-equilibrium albite dissolution as well (Arvidson and Lüttge, 2010).

Near-equilibrium log–log dissolution data plotted versus undersaturation, and their York fits, are presented in Fig. 7 and Table 4. Dissolution rates at replicate saturation states agree within error of each other. Our results give fitted values of n varying from 2.92 to 3.85 (Table 4). These large n values demonstrate a strongly nonlinear relationship between dissolution rate and undersaturation. This nonlinearity is more evident when a larger range of undersaturations are considered. In Fig. 9, we show near-equilibrium dissolution data plotted with two far-from-equilibrium experiments, along with the very near-equilibrium point discussed in Section 4.1. In order to plot all of these data, we have adjusted the undersaturation to make this near-equilibrium point undersaturated (changing Ω from 1.07 to 0.995). Dissolution rates are plotted versus free energy, using $\Delta G = RT\ln(\Omega)$ (Fig. 9). The temperature used was 294 K. When plotted as an ensemble, a definite curvature is noticeable, both far from equilibrium, and in the figure inset, very close to equilibrium as well. This is the type of curvature described by Arvidson and Lüttge (2010) and Xu et al. (2012). This curvature is further supported by fitting our data over narrow ranges of undersaturation: closer to equilibrium, a log–log regression gives a smaller n. Further from equilibrium, n grows larger. A similar feature is also noticeable in data from Keir (1980), especially in his reagent calcite and small size-fraction sedimentary data.

This curvature helps explain the range of n values determined for our 3 materials. It is also evidence for multiple dissolution mechanisms. Similar curvature has also been documented before by other mechanistic studies (Berner and Morse, 1974; Teng, 2004; Arvidson and Lüttge, 2010; Xu et al., 2012), and has been the subject of some debate. There is general agreement that strongly nonlinear dissolution behavior must be related to criticality in the mineral-solution system. In this scheme, there is some critical undersaturation, Ω_c, that once surpassed, allows dissolution to occur very rapidly. In a seminal study, Berner and Morse (1974) argued that near-equilibrium criticality was related to the abundance of phosphate ion adsorbed to the mineral surface. Berner and Morse hypothesized that these adsorbed ions prevent dissolution steps from propagating. Once below a certain threshold saturation state, however, dissolution is able to overcome these adsorbed barriers and a dissolution kink or step propagates very rapidly. Indeed, the zeta-potential of calcite is quite high (~9 at atmospheric pCO_2, Heberling et al. (2011)), which would implicate negatively charged ions as the barrier-forming species. This study represents new evidence for criticality at ΔG ~0.4–0.6 kJ/mol (Fig. 9). This criticality at very low free energy seems to be unique to seawater. The Ω_c given for step-edge propagation in freshwater (Teng, 2004; Xu et al., 2012) is around 0.3 (−2.9 kJ/mol), which is quite different from our findings. We calculate Ω_c using the equation from Berner and Morse (1974), which assumes that phosphate adsorption poisons the calcite surface and prevents step propagation. This calculation gives $\Omega_c \sim 0.9$, which is consistent with our curvature, phosphate ion concentration, and solid:solution ratio of our experiments. Although Walter and Burton (1986) showed little dependence of curvature on phosphate ion concentration, further work should be done on the role of low phosphate concentrations in calcite dissolution kinetics.

Dickson standard seawater is poisoned with mercuric chloride, so Hg^{2+} could also poison the calcite surface. There is evidence that Hg^{2+} does not appreciably adsorb onto calcite (Bilinski et al., 1991), and thus should not interfere with dissolution kinetics. There is also some evidence that magnesium ion could play a role in inhibiting step edge formation and propagation close to equilibrium (Xu and Higgins, 2011). These authors report an inhibitory effect at $\Omega_c = 0.2$, although their Ω is poorly constrained due to gas exchange considerations. There are two effects of magnesium on dissolution rate. The first is its effect on K'_{sp}. Overgrowth of calcite from seawater onto pure calcium carbonate would contain ~8 mole% magnesium (Mucci and Morse, 1984). This resulting overgrowth could have a different solubility than the original crystal. The second is an actual relationship with Ω_c through surface poisoning. Chemisorption of magnesium onto calcite could either prevent other species from attacking the mineral surface, or prevent steps from retreating (Xu and Higgins, 2011). If

magnesium were the cause of our observed criticality, this would imply that at seawater Mg concentrations (53 mmol/kg), Ω_c must shift towards equilibrium. This inference is rather counterintuitive, as it implies that magnesium ion's inhibitory effect changes sign somewhere between 1 and 50 mmol/kg. The solubility of Magnesian carbonates goes through a minimum at 4 mole%, and if the equilibrium composition of the solid displays such a reversal in seawater solutions of various Mg:Ca ratio, the multiple effects of Mg concentration on the calcite-seawater system could lead to such a sign reversal in the dissolution kinetics as well.

Finally, Zhang and Nancollas (1998), through a kinetic treatment of an ideal AB (i.e. two component) crystal, indicate that dissolution rates should also be strongly dependent on the ratio of calcium to carbonate ions. Over the range of undersaturations we explore here, that ratio does not vary much; it is fixed at around $[Ca^{2+}] : [CO_3^{2-}] \sim 300$. At a solution ratio of 100, Zhang and Nancollas (1998) showed a 40% change in the calcium-carbonate ion ratio correction function to their dissolution rate expression over a saturation range from 0 to 1. This change is small compared to the orders of magnitude change in rates we observe here. The solution ratio might be important in solutions with a wide range of calcium and carbonate ion concentrations, and could be worth further investigation with our method. But it is not an important factor in the nonlinearity of our dissolution rates close to equilibrium. We have not attempted to determine the underlying controls on criticality in the calcite-seawater system. An understanding of this criticality should elucidate the underlying mechanisms of calcite dissolution.

4.4. Specific rate constant, k

Our York-regression fits (Fig. 7, Table 4) show k-values ranging from 0.3 to $1.0 \cdot 10^{-3}$ g cm^{-2} day^{-1} for the different material types measured. Our specific rate constant, k_{geom}, is a measure of the far-from-equilibrium bulk dissolution rate in natural seawater, where Ω approaches 0, i.e. Rate $= k(1-0)^n = k$. We have two independent estimates of k_{geom}: a fit to our near-equilibrium data, extrapolated to $\Omega = 0$, and a true, far-from-equilibrium dissolution rate experiment run at $\Omega \sim 0.01$. A comparison of these two estimates of the rate constant to other measured dissolution rates in dilute solution is presented in Table 5. Surprisingly, all of these measured dissolution rates are within an order of magnitude of each other, and many even agree within error. These studies were all performed in different solutions, suggesting similar dissolution mechanisms far enough from equilibrium, regardless of ionic strength and other solution considerations. These studies also employ a wide range of measurement techniques. The pH-stat method, first employed by Morse and Berner (1972), was also employed by Plummer and Wigley (1976) in dilute solution. At near-neutral pH, they found no dependence of dissolution rate on pH. The closest analog to our experiments are those performed in seawater by Keir (1980), whose k is also presented in Table 5. With the exception of Keir's data, all rate constants here are normalized to geometric, not BET, surface area.

Our k does not agree well with that of Keir (1980) by at least a factor of 6; his rates, by his own admission, are quite fast (Keir, 1983) and do not compare well with *in situ* results (e.g. Honjo and Erez (1978)). This discrepancy could be due to incorrectly defined carbonate system parameters, although a refit of the data by Hales and Emerson (1997b) still gives a very large dissolution rate. Instead, the difference could be due to a difference in measured and actual saturation state. One other difference could be that once steady state was reached in Keir's flow-through reactor, there was enough dissolution to significantly change the mineral's surface area. This would lead to enhanced rates, since specific surface area increases as dissolution proceeds (Honjo and Erez, 1978), and dissolution rates can vary by orders of magnitude as the surface evolves in dissolution simulations (Luttge et al., 2013). Our measured far-from-equilibrium dissolution rate, on the other hand, is slightly on the upper end, but around the mean value of the dissolution rates in Table 5. An explanation for our elevated rate constant is that this experiment was conducted at a pH of about 5.5. At this pH, dissolution through direct hydrogen ion attack is proposed as a significant contributor to the overall dissolution rate, which could explain the elevated rate compared to that extrapolated from our near-equilibrium results (at pH ~7; Plummer and Wigley (1976), Sjöberg (1976)).

In the rotating disk experiments of Sjöberg and Rickard (1985), a strong dependence on calcium ion concentration is noted; they attribute this dependence to transport of calcium ion from the reacting mineral surface to the bulk solution. Their calculated dissolution rate at seawater-like calcium concentration (10 mM) is in excellent agreement with our calculated value of k. We will need to further investigate the effect of calcium ion concentration on dissolution rate if we are to determine if it plays a role in the chemical kinetics, above and beyond its effect on transport of calcium away from the mineral surface.

4.5. Implications for the calcite lysocline

Ideally, calcite dissolution rate measurements determined in the laboratory should be able to explain variations of calcite reactivity in the natural environment, and help explain the distribution of calcitic sediments in the ocean. However, there has been a long-standing disagreement between laboratory measurements and field-based observations. Our near-equilibrium dissolution rate constant determined for 70–100 μm Aldrich calcite (8.5%/day; Table 4) is within the range proposed by both Martin and Sayles (1996) and Hales and Emerson (1997a) for use in lysocline models with a nonlinear rate law. It is also close to the value obtained by Keir (1983) (16%/day) during his sediment bed experiments and a strongly nonlinear ($n = 4.5$) rate law formulation. It is in very close agreement with the rate constant used by Friis et al. (2006) to match global alkalinity distributions in a GCM simulation. Our dissolution rates also match quite well with those determined by Honjo

Table 5
A comparison of normalized, far from equilibrium, calcite dissolution rates. Details of the studies are listed. The dissolution rates presented for this study, Cubillas et al. (2005) and Keir (1980) are the far-from-equilibrium dissolution rate (the extrapolated dissolution rate constant from the data in the listed pH range). We also present our own measurements of the zero Ω dissolution rate.

Study	Method	pH	$[Ca^{2+}]$ (mmol kg^{-1})	Dissolution rate (mol cm^{-2} s^{-1})
Plummer and Wigley (1976)	pH-stat	5.5–7.0	0	$3.2 \cdot 10^{-10}$
Sjöberg and Rickard (1985)	Rotating disk reactor	6–8	0	$6.9 \cdot 10^{-10}$
Sjöberg and Rickard (1985)	Rotating disk reactor	6–8	10	$8.7 \cdot 10^{-11}$
Shiraki et al. (2000)	*in situ* AFM	7.6	0	$1.8 \cdot 10^{-10}$
Shiraki et al. (2000)	Ca^{2+} Flux	7.6	0-0.01	$3.1 \cdot 10^{-10}$
Cubillas et al. (2005)	Stirred-flow reactor	5.1–9.8	0.1	$1.8 \cdot 10^{-10}$
Keir (1980)	Flow-through reactor	7.1–7.3	10	$5.1 \cdot 10^{-10}$
This study	k_{geom}	7.1–7.3	10	$8.5 \cdot 10^{-11}$
	Low Ω expt.	5.5	10	$3.8 \cdot 10^{-10}$

and Erez (1978), measured in flow-through reactors suspended in the water column. At $\Omega = 0.75$, we calculate a dissolution rate of $3.4 \cdot 10^{-6}$ g/cm^2/day. Honjo and Erez measured a dissolution rate of $2.1 \cdot 10^{-6}$ g/cm^2/day. These agreements lend strong support to our rate determinations, and the application of our rate constant to dissolution kinetics in natural environments. Below, we apply our rate formulation to the natural environment, using a simple model.

One of the most distinctive features of ocean sediment distribution is the calcite lysocline. The lysocline is defined here as the depth range over which calcite-bearing sediments drop from $\sim 80 - 90\%$ $CaCO_3$ to $\sim 0\%$. This depth range is highly variable, and can often exceed 1 km (Berger, 1970; Biscaye et al., 1976; Kolla et al., 1976). The lysocline typically starts at about the calcite saturation horizon (defined as the depth where bottom water $\Omega = 1$, but some researchers have shown that the lysocline can start above (Emerson and Bender, 1981) or below (Archer, 1996; Archer, 1991) this horizon. Ever since the first measurements of $\%CaCO_3$ in ocean sediments , a major question has been: What controls the shape and position of the calcite lysocline? To first order, the bottom water saturation state should exert fundamental control on the sediment composition. If calcite response to this undersaturation is fast, the sedimentary composition will be controlled by a diffusive flux between a saturated boundary layer and the undersaturated bottom water. If the response is slow, the amount of calcite in sediments will be controlled by the kinetics of dissolution itself. Kinetic control has been long-favored in the literature (Morse and Berner, 1972), but there is also recent evidence for a transport-controlled lysocline (Boudreau et al., 2010a,b; Boudreau, 2013). In his latest estimates, Boudreau (2013) predicts lysocline thicknesses for two oceanic locations. However, his equations rely on a large diffusive boundary layer of ~ 1.2 mm, and is only able to fit rather narrow lysocline thicknesses of 300–500 m.

In order to test the influence of our current measured rates on the shape of the calcite lysocline, we constructed a simple model of $\%CaCO_3$, where the fraction of calcite in the top sediment layer, B_{CaCO_3} is calculated as:

$$B_{CaCO_3} = \frac{F_{rain} - F_{diss}}{F_{clay} + F_{rain} - F_{diss}}, \quad (6)$$

where F_{rain} is the flux of calcite rain to the seafloor, F_{diss} is the calcite dissolution flux, and F_{clay} is the flux of non-carbonate detritus to the seafloor, all in g/cm^2/kyr. We tested out end-member cases of diffusive and kinetic control by applying various forms of F_{diss}. In the case of transport (diffusive) control:

$$F_{diss} = \beta \cdot ([CO_3^{2-}]_{btm} - [CO_3^{2-}]_{sat}) \cdot \rho_{calc} \cdot \Delta h \cdot mm_{calc}, \quad (7)$$

where β is the mass transfer velocity in m/yr which relates the diffusivity of calcium and carbonate ions and the diffusive boundary layer thickness, $[CO_3^{2-}]_{btm}$ is the bottom water carbonate ion concentration which we assume to be 100 μmol/kg, and $[CO_3^{2-}]_{sat}$ is the calcite saturation value of carbonate ion, parameterized as a function of depth as in Boudreau et al. (2010b). $\rho_{calcite} = 2.7$ g/cm^3 is the density of calcite, Δh is the depth of available sediment for dissolution (here assumed to be 1 cm), and $mm_{calc} = 100$ g/mol is the molar mass of calcium carbonate. We chose to model this diffusive flux for two different boundary layer thicknesses; one from Boudreau (2013) ($\beta = 12.7$ m/yr; 1.2 mm boundary layer thickness) and one from Santschi et al. (1983) (32.1 m/yr; 475 μm). The diffusive fluxes and percent calcium carbonate for these fluxes are given in Fig. 10a and b, respectively.

For kinetic control, the rate is parameterized as:

$$F_{diss} = [CaCO_3]_{stock} \cdot k_{diss} \cdot (1 - \Omega)^n; \quad (8)$$

where $[CaCO_3]_{stock} = \frac{F_{rain}}{F_{clay}+F_{rain}} \cdot (1 - \phi) \cdot \rho_{calcite}$ is the inventory of solid calcite at the sediment-water interface. ϕ is the porosity, assumed to be 0.8, and $\rho_{calcite}$ is 2.7 g/cm^3. k_{diss} in this case is in units of g/g/kyr, or kyr^{-1}. We compared three different rate parameterizations. First is the rate chosen by Hales and Emerson (1997b) that provided the best fit to Ontong-Java Plateau sediments ($n = 1$, $k_{diss} = 0.1\%$/day). Second is the rate constant chosen by Boudreau (2013) that provides the best linear fit to the data from Keir (1983) (60 g cm^{-2} kyr^{-1}). Third is our rate constant data, where $n = 3.85$ and $k_{diss} = 0.085$ g/g/day, the best fit to our near-equilibrium 70–100 μm size fraction calcite. These dissolution fluxes and associated percent calcium carbonate curves are presented with the diffusive model results in Fig. 10a and b, respectively. Both transport-only fluxes produce relatively shallow lysoclines,

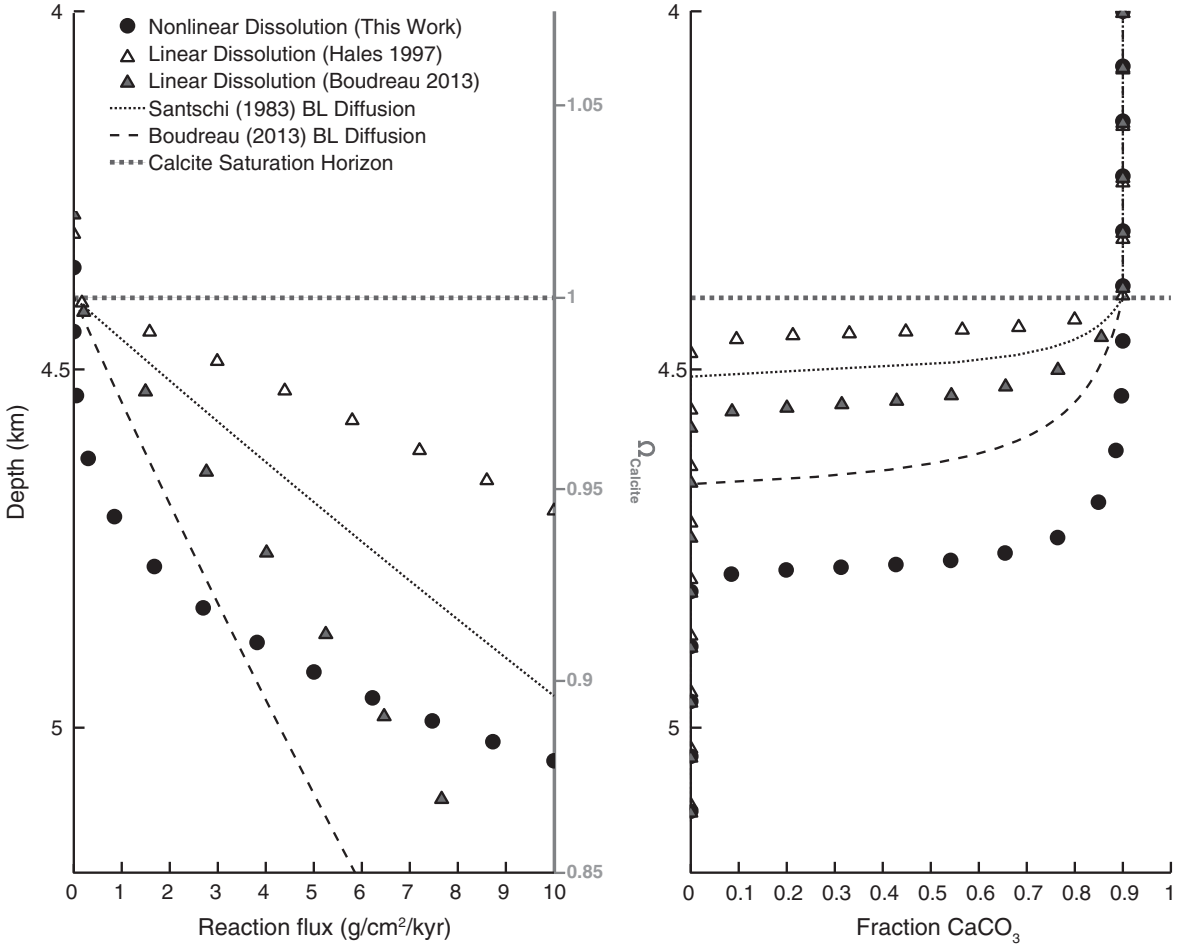

Fig. 10. A simple model of the calcite lysocline (see text for the model and numbers used). (a) Dissolution fluxes parameterized as either diffusive (dashed lines) or kinetic (symbols). Depth is converted to Ω as in the model, and is plotted on the *y*-axis for reference. (b) $\%_{CaCO_3}$ using the dissolution fluxes from (a).

which initiate immediately at the saturation horizon. Different dissolution fluxes produce a range of behaviors, with linear rate laws producing very shallow lysoclines. Our data shows a large offset in water column depth between a drop in B_{CaCO_3} and the saturation horizon.

Given the observations of $\%CaCO_3$ in surface sediments, and our measured dissolution rates, there must be other factors that contribute to the shape of the lysocline. First of all, our dissolution flux crosses the transport-only flux predicted by Boudreau (2013). After this crossover at a depth of ~ 4.8 km, the dissolution rate outpaces the rate of solute transport. The sediment composition would reflect this switch, and preserve more calcite than with kinetics alone, making transport the limiting term in calcite dissolution, and further deepening the lysocline.

In this simple model, we have explicitly ignored any porewater reactions taking place, such as diffusion of DIC species, sediment compaction, bioturbation, and respiration of organic matter. There is much evidence for respiration-driven dissolution in deep-sea sediments (Emerson and Bender, 1981; Hales, 2003; Dunne et al., 2012). Respiration in sediments would drive down the saturation state due to excess CO_2, which would in turn have a large effect on the dissolution rate in the case of a nonlinear rate response to undersaturation. Respiration-driven dissolution is largely ignored in the lysocline model of Boudreau (2013). Since we have conclusively documented a nonlinear dissolution response, our results imply a potentially large role of respiration-driven dissolution, and also could allow for a switch in kinetic- to transport-controlled dynamics of the chemical lysocline.

5. CONCLUSIONS

We demonstrate here a new technique for measuring calcium carbonate dissolution rates, based on an isotopic tracer methodology. This method allows for unprecedented control on saturation state and mineral surface area. Geometric normalization of different grain sizes aligns all data onto a single curve, although the small offset between the Aldrich and our gel-grown calcites could be due to differences is surface morphology and microstructure. The near-equilibrium dissolution rates are fit by the empirical equation:

$$\text{Rate } (\text{g/cm}^2/\text{day}) = 7.2 \pm 0.6 \cdot 10^{-4}(1-\Omega)^{3.9\pm0.1}.$$

This relationship is descriptive; it implies at least two fundamental dissolution mechanisms, as well as criticality in dissolution response to undersaturation. Furthermore, our dissolution rate constants agree quite well with far-from-equilibrium dissolution rates, determined over a range of conditions and methodologies. Finally, we demonstrate for the first time agreement between our laboratory-determined dissolution rates, and those measured or extrapolated from field data. Observations of calcite sediments, paired with our rate determinations, suggest that both transport and kinetics play a role in setting $\%CaCO_3$. Respiration-driven dissolution is likely an important process as well.

ACKNOWLEDGEMENTS

The authors would like to acknowledge Eric Kleinsasser and Joel Schmidt for help with BET analysis, and Burke Hales for helpful suggestions regarding the solubility of calcites. We also thank the three anonymous reviewers for their comments and criticisms on the original manuscript drafts. This work was supported by an NSF Ocean Acidification grant (numbers OCE1220600 and OCE1220302) and the NSF Graduate Research Fellowship.

REFERENCES

Arakaki T. and Mucci A. (1995) A continuous and mechanistic representation of calcite reaction-controlled kinetics in dilute solutions at 25 C and 1 atm total pressure. *Aquat. Geochem.* **1**, 105–130.

Archer D. (1991) Modeling the calcite lysocline. *J. Geophys. Res. Oceans (1978–2012)* **96**(C9), 17037–17050.

Archer D. E. (1996) An atlas of the distribution of calcium carbonate in sediments of the deep sea. *Global Biogeochem. Cycles* **10**(1), 159–174.

Archer D., Kheshgi H. and Maier-Reimer E. (1998) Dynamics of fossil fuel CO_2 neutralization by marine $CaCO_3$. *Global Biogeochem. Cycles* **12**(2), 259–276.

Arvidson R. S. and Lüttge A. (2010) Mineral dissolution kinetics as a function of distance from equilibrium – new experimental results. *Chem. Geol.* **269**(1-2), 79–88.

Badillo-Almaraz V. E. and Ly J. (2003) Calcium sorption on hydroxyapatite in aqueous solutions: reversible and nonreversible components. *J. Colloid Interface Science* **258**(1), 27–32.

Bednarsek N., Feely R. A., Reum J. C. P., Peterson B., Menkel J., Alin S. R. and Hales B. (2014) Limacina helicina shell dissolution as an indicator of declining habitat suitability owing to ocean acidification in the California Current Ecosystem. *Proc. R. Soc. B Biol. Sci.* **281**(1785), 20140123.

Berelson W. M., Balch W. M., Najjar R., Feely R. A., Sabine C. and Lee K. (2007) Relating estimates of $CaCO_3$ production, export, and dissolution in the water column to measurements of $CaCO_3$ rain into sediment traps and dissolution on the sea floor: a revised global carbonate budget. *Global Biogeochem. Cycles* **21**(1).

Berger W. H. (1970) Planktonic foraminifera – selective solution and lysocline. *Marine Geol.* **8**(2), 111–138.

Berner R. A. and Morse J. W. (1974) Dissolution kinetics of calcium carbonate in sea water; IV, theory of calcite dissolution. *Am. J. Sci.* **274**, 108–134.

Bilinski H., Kozar S., Plavšić M., Kwokal Ž. and Branica M. (1991) Trace metal adsorption on inorganic solid phases under estuarine conditions. *Marine Chem.* **32**(2-4), 225–233.

Biscaye P. E., Kolla V. and Turekian K. K. (1976) Distribution of calcium carbonate in surface sediments of the Atlantic Ocean. *J. Geophys. Res. Oceans (1978–2012)* **81**(15), 2595–2603.

Boudreau B. P. (2013) Carbonate dissolution rates at the deep ocean floor. *Geophys. Res. Lett.* **40**(4), 744–748.

Boudreau B. P., Middelburg J. J., Hofmann A. F. and Meysman F. J. R. (2010a) Ongoing transients in carbonate compensation. *Global Biogeochem. Cycles* **24**(4).

Boudreau B. P., Middelburg J. J. and Meysman F. J. R. (2010b) Carbonate compensation dynamics. *Geophys. Res. Lett.* **37** (L03603), 1–5.

Brunauer S., Emmett P. H. and Teller E. (1938) Adsorption of gases in multimolecular layers. *J. Am. Chem. Soc.* **60**, 309–319.

Cubillas P., Köhler S., Prieto M., Chaïrat C. and Oelkers E. H. (2005) Experimental determination of the dissolution rates of calcite, aragonite, and bivalves. *Chem. Geol.* **216**(1-2), 59–77.

de Kanel J. and Morse J. W. (1979) A simple technique for surface area determination. *J. Phys. E Sci. Instrum.* **12**, 272–273.

Dickson A. G. (2009) The carbon dioxide system in seawater: equilibrium chemistry and measurements. In *Guide to Best Practices for Ocean Acidification Research and Data Reporting* (eds. U. Riebesell, V. J. Fabry and L. Hansson). Publications Office of the European Union, Luxembourg.

Dickson A. G. and Millero F. J. (1987) A comparison of the equilibrium constants for the dissociation of carbonic acid in seawater media. *Deep Sea Res.* **34**(10), 1733–1743.

Dunne J. P., Hales B. and Toggweiler J. R. (2012) Global calcite cycling constrained by sediment preservation controls. *Global Biogeochem. Cycles* **26**(3).

Emerson S. and Bender M. (1981) Carbon fluxes at the sediment-water interface of the deep-sea: calcium carbonate preservation. *J. Marine Res.* **39**, 139–162.

Feely R. A., Sabine C. L., Byrne R. H., Millero F. J., Dickson A. G., Wanninkhof R., Murata A., Miller L. A. and Greeley D. (2012) Decadal changes in the aragonite and calcite saturation state of the Pacific Ocean. *Global Biogeochem. Cycles* **26**(3).

Fischer C., Arvidson R. S. and Lüttge A. (2012) How predictable are dissolution rates of crystalline material? *Geochim. Cosmochim. Acta* **98**(C), 177–185.

Friis K., Najjar R. G., Follows M. J. and Dutkiewicz S. (2006) Possible overestimation of shallow-depth calcium carbonate dissolution in the ocean. *Global Biogeochem. Cycles* **20**(4).

Fukuhara T., Tanaka Y., Ioka N. and Nishimura A. (2008) An in situ experiment of calcium carbonate dissolution in the central Pacific Ocean. *Int. J. Greenhouse Gas Control* **2**(1), 78–88.

Gehlen M., Bassinot F. C., Chou L. and McCorkle D. (2005a) Reassessing the dissolution of marine carbonates: I. Solubility. *Deep Sea Res. Part I* **52**(8), 1445–1460.

Gehlen M., Bassinot F. C., Chou L. and McCorkle D. (2005b) Reassessing the dissolution of marine carbonates: II. Reaction kinetics. *Deep Sea Res. Part I* **52**(8), 1461–1476.

Hales B. (2003) Respiration, dissolution, and the lysocline. *Paleoceanography* **18**(4).

Hales B. and Emerson S. (1997a) Calcite dissolution in sediments of the Ceara Rise: in situ measurements of porewater O_2, pH, and $CO_{2(aq)}$. *Geochim. Cosmochim. Acta* **61**(3), 501–514.

Hales B. and Emerson S. (1997b) Evidence in support of first-order dissolution kinetics of calcite in seawater. *Earth Planet. Sci. Lett.* **148**, 317–327.

Heberling F., Trainor T. P., Lützenkirchen J. and Eng P. (2011) Structure and reactivity of the calcite–water interface. *J. Colloid Interface Sci.* **354**, 843–857.

Honjo S. and Erez J. (1978) Dissolution rates of calcium carbonate in the deep ocean; an in-situ experiment in the North Atlantic Ocean. *Earth Planet Sci. Lett.* **40**, 287–300.

Ilyina T. and Zeebe R. E. (2012) Detection and projection of carbonate dissolution in the water column and deep-sea sediments due to ocean acidification. *Geophys. Res. Lett.* **39**.

Keir R. S. (1980) The dissolution kinetics of biogenic calcium carbonates in seawater. *Geochim. Cosmochim. Acta* **44**, 241–252.

Keir R. S. (1983) Variation in the carbonate reactivity of deep-sea sediments: determination from flux experiments. *Deep Sea Res.* **30**(3A), 279–296.

Kolla V., Bé A. W. H. and Biscaye P. E. (1976) Calcium carbonate distribution in the surface sediments of the Indian Ocean. *J. Geophys. Res. Oceans (1978–2012)* **81**(15), 2605–2616.

Kontoyannis C. G. and Vagenas N. V. (2000) Calcium carbonate phase analysis using XRD and FT-Raman spectroscopy. *The Analyst* **125**(2), 251–255.

Lueker T. J., Dickson A. G. and Keeling C. D. (2000) Ocean pCO_2 calculated from dissolved inorganic carbon, alkalinity, and equations for K_1 and K_2: validation based on laboratory measurements of CO_2 in gas and seawater at equilibrium. *Marine Chem.* **70**(1-3), 105–119.

Luttge A., Arvidson R. S. and Fischer C. (2013) A stochastic treatment of crystal dissolution kinetics. *Elements* **9**(3), 183–188.

MacInnis I. N. and Brantley S. L. (1992) The role of dislocations and surface morphology in calcite dissolution. *Geochim. Cosmochim. Acta* **56**(3), 1113–1126.

Martin W. R. and Sayles F. L. (1996) $CaCO_3$ dissolution in sediments of the Ceara Rise, western equatorial Atlantic. *Geochim. Cosmochim. Acta* **60**(2), 243–263.

Mehrbach C., Culberson C. H., Hawley J. E. and Pytkowicz R. M. (1973) Measurement of the apparent dissociation constants of carbonic acid in seawater at atmospheric pressure. *Limnol. Oceanogr.* **18**(6), 897–907.

Morse J. W. and Berner R. A. (1972) Dissolution kinetics of calcium carbonate in seawater; II. A kinetic origin for the lysocline. *Am. J. Sci.* **272**, 840–851.

Morse J. W., Mucci A. and Millero F. J. (1980) The solubility of calcite and aragonite in seawater of 35‰ salinity at 25 C and atmospheric pressure. *Geochim.Cosmochim. Acta* **44**, 85–94.

Mucci A. (1983) The solubility of calcite and aragonite in seawater at various salinities, temperatures, and one atmosphere total pressure. *Am. J. Sci.* **283**, 780–799.

Mucci A. and Morse J. W. (1984) The solubility of calcite in seawater solutions of various magnesium concentration, I_t= 0.697 at 25 and one atmosphere total pressure. *Geochim. Cosmochim. Acta* **48**, 815–822.

Nickl H. J. and Henisch H. K. (1969) Growth of calcite crystals in gels. *J. Electrochem. Soc. Solid State Sci.* **116**(9), 1258–1260.

Plummer L. N. and Wigley T. (1976) The dissolution of calcite in CO_2-saturated solutions at 25 °C and 1 atmosphere total pressure. *Geochim. Cosmochim. Acta* **40**(2), 191–202.

Sabine C. L., Feely R. A., Gruber N., Key R. M., Lee K., Bullister J. L., Wanninkhof R., Wong C. S., Wallace D., Tilbrook B., Millero F. J., Peng T. H., Kozyr A., Ono T. and Rios A. F. (2004) The oceanic sink for anthropogenic CO_2. *Science* **305** (5682), 367–371.

Santschi P. H., Nyfeller U. P., Bower P., Azevedo A. and Broecker W. S. (1983) Estimates of the resistance to chemical-transport posed by the deep-sea boundary-layeri. *Limnol. Oceanogr.* **28** (5), 899–912.

Sarmiento J. and Gruber N. (2006) *Ocean Biogeochemical Dynamics*. Princeton University Press.

Schwartz A., Eckart D., O'Connell J. and Francis K. (1971) Growth of vaterite and calcite crystals in gels. *Mater. Res. Bull.* **6**, 1341–1344.

Shiraki R., Rock P. A. and Casey W. H. (2000) Dissolution kinetics of calcite in 0.1 M NaCl solution at room temperature: an atomic force microscopic (AFM) study. *Aquat. Geochem.* **6**, 87–108.

Sigman D. M. and Boyle E. A. (2000) Glacial/interglacial variations in atmospheric carbon dioxide. *Nature* **407**(6806), 859–869.

Sjöberg E. L. (1976) A fundamental equation for calcite dissolution kinetics. *Geochim. Cosmochim. Acta* **40**(4), 441–447.

Sjöberg E. L. and Rickard D. T. (1984) Calcite dissolution kinetics – surface speciation and the origin of the variable pH-dependence. *Chem. Geol.* **42**(1-4), 119–136.

Sjöberg E. L. and Rickard D. T. (1985) The effect of added dissolved calcium on calcite dissolution kinetics in aqueous solutions at 25 C. *Chem. Geol.* **49**(4), 405–413.

Stockner T., Qin D., Plattner G., Tignor M., Allen S., Boschung J., Nauels A., Xia Y., Bex V. and Midgley P. (2013). *Climate Change 2013: The Physical Science Basis*. Contribution of Working Group I to the Fifth Assessment Report of the Intergovernmental Panel on Climate Change. Tech. rep.

Tang R., Orme C. A. and Nancollas G. H. (2004) Dissolution of crystallites: surface energetic control and size effects. *ChemPhysChem* **5**(5), 688–696.

Teng H. H. (2004) Controls by saturation state on etch pit formation during calcite dissolution. *Geochim. Cosmochim. Acta* **68**(2), 253–262.

Tertre E., Beaucaire C., Juery A. and Ly J. (2010) Methodology to obtain exchange properties of the calcite surface–application to major and trace elements: Ca(II),HCO_3^-, and Zn(II). *J. Colloid Interface Sci.* **347**(1), 120–126.

Walter L. M. and Burton E. A. (1986) The effect of orthophosphate on carbonate mineral dissolution rates in seawater. *Chem. Geol.* **56**, 313–323.

Xu M. and Higgins S. R. (2011) Effects of magnesium ions on near-equilibrium calcite dissolution: step kinetics and morphology. *Geochim. Cosmochim. Acta* **75**, 719–733.

Xu J., Fan C. and Teng H. H. (2012) Calcite dissolution kinetics in view of Gibbs free energy, dislocation density, and pCO_2. *Chem. Geol.* **322–323**(C), 11–18.

York D. (1966) Least-squares fitting of a straight line. *Can. J. Phys.* **44**(5), 1079–1086.

Zhang J. and Nancollas G. H. (1998) Kink density and rate of step movement during growth and dissolution of an AB crystal in a nonstoichiometric solution. *J. Colloid Interface Sci.* **200**(1), 131–145.

Associate Editor: Robert H. Byrne